Quantifying the large contribution from orbital Rashba-Edelstein effect to the effective damping-like torque on magnetization

S. Krishnia,[1,*] B. Bony,[1] E. Rongione,[1] L. Moreno Vicente-Arche,[1] T. Denneulin,[2] A. Pezo,[1] Y. Lu,[2] R. E. Dunin-Borkowski,[2] S. Collin,[1] A. Fert,[1] J.-M. George,[1] N. Reyren,[1] V. Cros,[1,†] and H. Jaffrès[1,‡]

[1] *Laboratoire Albert Fert, CNRS, Thales, Université Paris-Saclay, 91767, Palaiseau, France*
[2] *Ernst Ruska-Centre for Microscopy and Spectroscopy with Electrons (ER-C 1) and Peter Grünberg Institut (PGI-5), Forschungszentrum Jülich GmbH, 52425 Jülich, Germany*

(Dated: March 11, 2024)

I. XPS MEASUREMENTS

The XPS measurements were carried out with the main objective of obtaining information about the spontaneously formed oxide layer in Co|Cu*, Co|Pt|Cu* and Pt|Co|Cu|Al* (where "*" denotes that the top layer was exposed to air"). More specifically, through these XPS measurements, we do expect to support the results obtained on Cu* samples, which suggest the presence of a Cu/CuOx interface acting as a source of orbital angular momentum (OAM) by means of the orbital Rashba-Edelstein effect (OREE); also with the same purpose, we aim to confirm the presence of a metallic Cu/Al interface for samples with Al*.

In details, X-ray photoemission spectroscopy (XPS) has been performed in a UHV chamber with a base pressure of about $3.5e^{-9}$ mbar. All spectra were obtained using a non-monochromatic Mg-Kα radiation source with an excitation energy of 1253.6 eV. The charge correction has been performed using adventitious carbon, *i.e.*, we consider the principal component of the C 1*s* peak at 284.8 eV. Spectra have been collected through a hemispherical analyser working in CAE mode with a step energy of 60 eV, a step size of 0.2 eV and a dwelling time of 0.1 s. Finer sweeps have been performed in the energy ranges of interest with a step energy of 20 eV, a step size of 0.05 eV and a dwelling time of 0.5 s. For better comparison, the number of iterations and energy range of the spectra has been kept constant. Further, most of the spectra have been y-shifted while keeping the relative intensities comparable, *i.e.*, the intensities have been factored only in cases specified in figure captions.

The discussion of results has been sorted according to the presence of Cu* or Al* in the samples. For Cu* samples, we will perform a qualitative interpretation of the reference spectra and a study of both the compositional gradient by angle-dependent XPS measurements and samples with different thicknesses. Due to several factors such as the instability of the Cu* overlayer during XPS measurements (under X-ray exposure in UHV) and the already complex differentiation of some Cu species by XPS [1, 2], we consider that a quantitative study requires a more extensive and systematic study with greater control over the samples. In contrast, the spectra obtained for Pt|Co|Cu|Al* allow us to proceed with a quantitative analysis due to their lower complexity.

A. Co|Cu* and Co|Pt|Cu* series

1. *Reference spectra*

The *in situ* connection of our XPS with the sputtering chamber allows us to take reference spectra for a Cu film without breaking the vacuum. The spectra in Fig. 1 show the photoemission lines: Cu 2p (a) and O 1s (b), as well as the Auger transition $L_3M_{4,5}M_{4,5}$ (c). According to previous studies [1–3], the spectra obtained *in situ* (blue) can be used as a reference for metallic Cu given the peak-shape of the Auger transition $L_3M_{4,5}M_{4,5}$ (c). However, we also noticed a weak shake-up structure in the Cu 2p region (a) and a small component in the O 1s region (b), which could be ascribed to the presence of adsorbates on the as-sputtered Cu surface.

On the other hand, *ex situ* spectra (orange) have been collected after exposure to normal conditions (*i.e.*, ambient P and T) for approximately 5 min. These spectra show a slight shift of the maxima towards lower binding energies in the Cu 2p region (a), a clear contribution arising at about 530.2 eV in the O 1s energy range (b) and a very different

* Current address: Institute of Physics, Johannes Gutenberg University Mainz, 55099 Mainz, Germany
† vincent.cros@cnrs-thales.fr
‡ henri.jaffres@cnrs-thales.fr

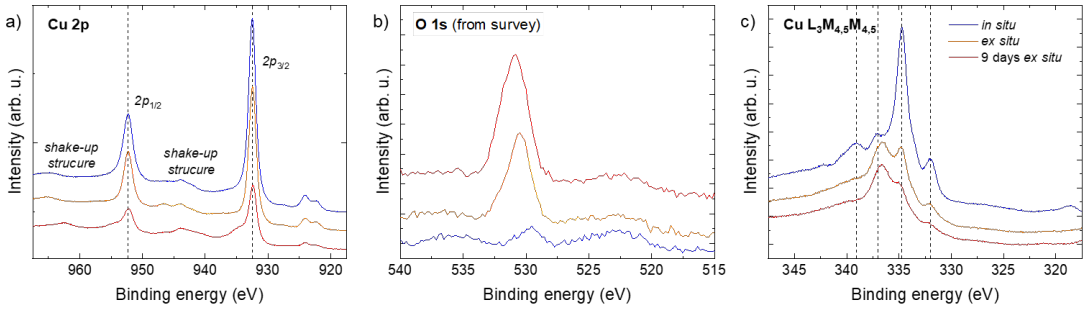

Figure 1. Reference XPS spectra of Cu for the Cu 2p (a) and O 1s (b) photoemission lines, as well as for the Auger $L_3M_{4,5}M_{4,5}$ transition (c), obtained *in situ* (blue), and after short (orange) and long (red) exposures at ambient pressure and temperature.

spectrum for the Auger transition $L_3M_{4,5}M_{4,5}$ (c) which shows a new component emerging at about 336.7 eV. We find that, after a short exposition to air, these spectra (in orange) are consistent with an oxidation of the sample surface from Cu to Cu_2O [1, 2, 4]. Note that Cu_2O is the only oxygenated compound expected in Cu* with a lower binding energy than metallic Cu for Cu $2p_{3/2}$ ($\simeq$932.4 eV), and thus able to explain the slight shift of the photoemission maximum towards lower binding energies.

However, although we found that the main oxidation product is Cu_2O, we cannot rule out the presence of other oxides such as CuO at very low concentration given the small energy splitting of the photoemission lines (Cu $2p_{3/2}$ $\simeq$ 933.6 eV, and O 1s $\simeq$ 529.4 eV) [1, 5]. Moreover, a mere presence of adsorbates such as hydroxides ($Cu(OH)_2$) and/or carbonates ($CuCO_3$) could also be overlooked in the Cu 2p region (a) and account not only for the stronger shake-up structure observed in panel (a), but also for the slight asymmetry of the O 1s peak in (b) (*i.e.*, its longer tail toward higher binding energies).

Spectra obtained after 9 days *ex situ* in normal conditions (red) show an even higher oxidation of Cu. In this case, the concentration of species with higher binding energy in both Cu 2p (a) and O 1s (b) regions increases, while the characteristic features of the metallic phase marked by dashed lines in the $L_3M_{4,5}M_{4,5}$ spectrum (c) are further smoothed out. Among the most likely species in spontaneously oxidized Cu, that can give a Cu $2p_{3/2}$ component around 934.0 eV and O 1s components with higher binding energy than Cu_2O, we find hydroxides ($Cu(OH)_2$) and carbonates ($CuCO_3$) [1, 5, 6].

In summary, the growth of a thick Cu film has allowed us to obtain reference spectra for metallic Cu films (blue), with lower (orange) and higher (red) degree of oxidation. Although we identified Cu_2O as the main product during early oxidation stages, we also found indications of $Cu(OH)_2$ and/or $CuCO_3$ at later stages. Also relevant to the study presented below is the possibility to distinguish the presence of metallic Cu from the Auger spectrum in (c), since its characteristic features (marked by dashed lines in (c)) are still visible after oxidation.

2. *Compositional gradient by angle-dependent XPS measurements*

In order to study the species distribution within the Cu* overlayer in Co|Cu* and Co|Pt|Cu* stacks, we performed an XPS study as a function of the take-off angle (TOA) of emitted photoelectrons. This TOA denotes the angle between the sample surface and the collection axis of the spectrometer. Accordingly, TOA90 is equivalent to normal emission (maximum probing depth) and TOA30 is equivalent to our geometry with a higher degree of inclination (minimum probing depth). Thus, if there is a compositional gradient within the Cu* overlayer, the contribution of near-surface species to the spectrum will be largest for the geometry with the shallower probing depth (*i.e.*, TOA30).

In the following sections, we will discuss the results obtained after performing the angular dependence for Co(2)|Pt(2)|Cu(3)*, where the number in parentheses is the thickness in nanometers. First, we will interpret the spectra obtained *in situ*, *i.e.*, without breaking the UHV conditions between measurements. Secondly, to address the observed Cu* reduction during these experiments, we will discuss the results obtained after exposing the samples to air for 3 days between XPS measurements. Note that, although we only show the results for Co(2)|Pt(2)|Cu(3)*, the same angle-dependence study was performed for Co(2)|Cu(3)* yielding a very similar understanding.

In situ XPS measurements - Cu* reduction under X-ray exposure in UHV

Fig. 2 shows the XPS spectra obtained for Co(2)|Pt(2)|Cu(3)*. It is important to highlight that these spectra were collected consecutively by keeping the sample in UHV, which, together with cumulative x-ray exposure, causes the Cu* overlayer to degrade significantly over time. This fact renders the spectra in Fig. 2 not comparable with each other, and suggests the need for a more systematic process, especially if the aim is a quantitative study of the compositional gradient and comparison between samples and/or material systems.

The Cu 2p and O 1s photoemission lines, as well as the $L_{2,3}M_{4,5}$ Auger transition, are shown respectively in panels (a), (b) and (c) of Fig. 2 for different TOA. Note that the sequence of measurements in time is indicated by the direction of the arrow in (b), while the colour code used for all spectra is shown in (c). Panels (a), (b) and (c) show a general trend as we increase the take-off angle. As expected for increasing probing depth (→TOA90), the contribution of hydroxides and/or carbonates to the spectrum decreases (a) while the characteristic features of metallic Cu emerge in the Auger spectrum (c). Also, we find that the photoemission maximum in the O 1s region shifts toward lower binding energies, suggesting that Cu_2O is farther from the surface than hydroxides and/or carbonates and, therefore, a spatial distribution within the Cu* overlayer as Cu|Cu_2O|$Cu(OH)_2$. However, panel (d) compares the first and last Cu 2p spectra obtained at normal emission and shows that the Cu* overlayer has been severely degraded during the XPS measurements. Therefore, the evolution of the spectra as a function of TOA should not be entirely attributed to a compositional gradient within the Cu* overlayer, as this could be magnified by the degradation of the Cu* overlayer, as well as by the direction in which the angular dependence has been performed (*i.e.*, we are measuring a more reduced sample as we increase the probing depth).

As for the degradation process, it could be interpreted from the Cu 2p (a) spectra as the transformation of Cu hydroxides into species with lower binding energy, such as CuO, Cu_2O or metallic Cu. However, the formation of these products is not inferred from the Auger (e) spectra, which remains similar after degradation. On the other hand, the decreasing intensity and the shift of the maximum in the O 1s region towards lower binding energies (b) rather suggest a decomposition of Cu hydroxides by desorption (H+ and/or OH-) than its transformation into CuO and/or Cu_2O.

In addition, we observed a partial charging effect with respect to the O 1s component for the last spectra obtained after a long X-ray exposure (last TOA90). That is, we find that our charge reference (C 1s peak at 284.8 eV) is no longer valid for photoemission lines with higher binding energy than the O 1s component (included), while it remains valid for those with lower binding energy. More specifically, by considering C 1s as a charge reference over the entire energy range, we observe a sudden shift of about 2 eV towards lower binding energies in the Cu 2p and O 1s region, resulting in unexpected binding energy values. Only for this case, the charge correction for the Cu 2p and O 1s spectra has been performed by correlating in energy values the signal coming from the sample holder (*i.e.*, the Fe 2p photoemission line) with previous measurements, resulting in a good fit with the evolution of the spectra collected so far.

In order to explain this phenomenon, we consider the possible energy loss of photoelectrons with higher kinetic energy (than those for the O 1s line) when participating in the ionisation of products obtained during Cu* degradation, *e.g.*, CuOOH-. Moreover, we found that the formation of such products during the degradation process could explain the contradictions between spectra. That is, the transformation of $Cu(OH)_2$ into CuOOH- would not imply a large variation in the relative concentration of species and could be unnoticed in the Auger spectrum (c), whereas it could give components in the Cu 2p spectrum with a lower binding energy (a).

In summary, from angle-dependent in situ XPS measurements we have found a Cu/Cu_2O/Cu(OH)2 compositional gradient in Co(2)|Pt(2)|Cu(3)* and Co(2)|Cu(3)* samples. However, we have also found evidence of degradation over time of the Cu* layer due to long exposure to x-rays and UHV, suggesting that this gradient is magnified. Moreover, we encountered that the degradation process could involve the formation of products such as CuOOH-, rarely considered during previous XPS studies and whose identification by XPS is certainly challenging. Undoubtedly, the degradation of the Cu* overlayer questions these results and implies the need to search for a more appropriate method to study the compositional gradient in Cu* systems.

Ex situ XPS measurements – a more reliable study

In order to address the degradation of the Cu* overlayer, angle-dependent XPS measurements were performed after exposing the samples to ambient conditions for 3 days between successive measurements (*i.e.*, allowing the Cu* overlayer to reoxidize).

Fig. 3 shows the spectra for Co(2)|Pt(2)|Cu(3)* following the opposite sequence of measurements (TOA90→TOA30). Therefore, to see if the sample has recovered the initial oxidation state, we can directly compare the first mea-

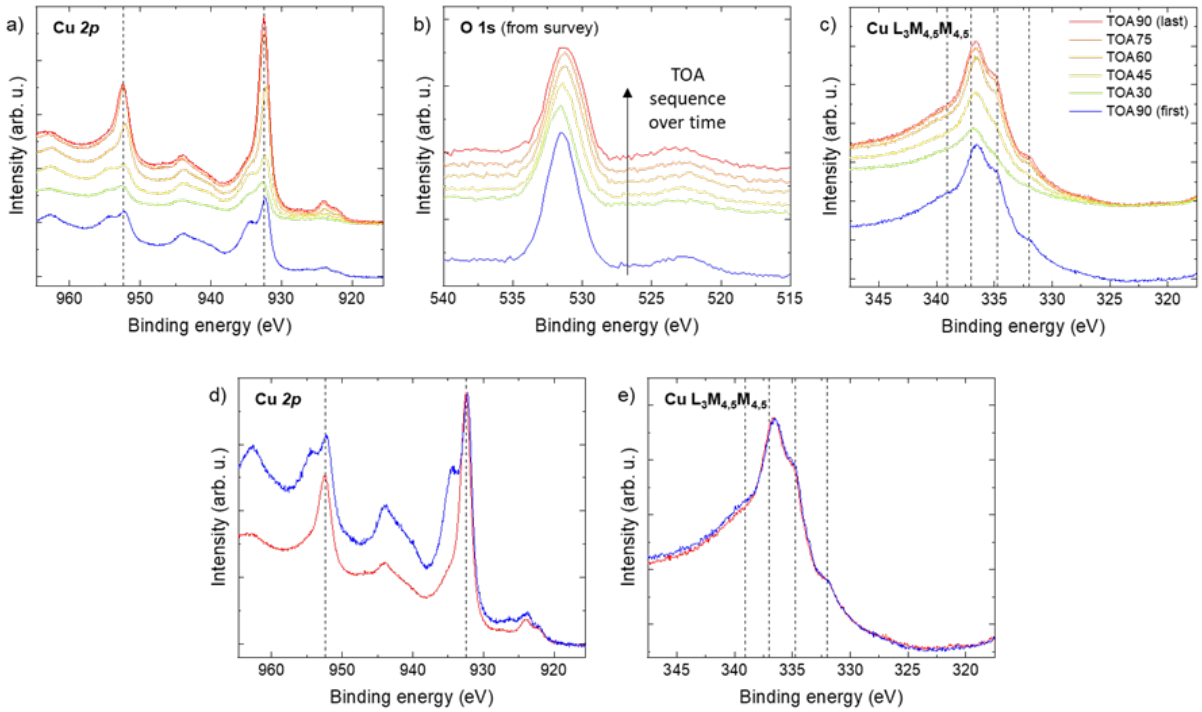

Figure 2. Take-off angle (TOA) dependence of XPS spectra collected in situ for Co(2)|Pt(2)|Cu(3)* sample in the energy ranges Cu 2p (a), O 1s, and the Auger $L_3M_{4,5}$ transition (c). The probing depth increases with TOA being maximum for TOA90. The time sequence of the measurements is shown in (b). The color code for all panels is shown in (c). Panels (d) and (e) compare the first (blue) and last (red) spectra at TOA90 for Cu 2p and the Auger $L_3M_{4,5}$ transition, respectively. The intensity of these spectra has been normalized for better comparison.

surement at normal emission in panel (d) of Fig. S2 (first TOA90, in blue) with the first measurement at normal emission in panel (d) of Fig. 3 (TOA90, in red). From this comparison, it can be inferred that the contribution of oxidised Cu species is significantly higher in Fig. S2 than in Fig. S3. Considering that the exposure time to ambient P and T has been 10 days for this case, we can state that this time was not sufficient to recover the initial oxidation state of Cu*, or that the Cu* overlayer was irreversibly affected by our first XPS measurements.

Panels (a), (b) and (c) show a general trend as we increase the take-off angle. Again, as expected for decreasing probing depth (TOA30), the contribution of hydroxides and/or carbonates to the spectrum increases (a) while the characteristic features of metallic Cu are smoothed out in the Auger spectrum (c). Also, we find that the photoemission maximum in the O 1s region shifts toward higher binding energies, suggesting that Cu_2O is farther from the surface than hydroxides and/or carbonates. Therefore, these spectra is also in good agreement with a spatial distribution within the Cu(3)* overlayer as $Cu|Cu_2O|Cu(OH)_2$.

3. Comparison of samples with different metal deposited thicknesses

In this section, we compare the spectra obtained at normal emission for samples with different thicknesses in Co|Pt|Cu* and Co|Cu* systems. These spectra are shown in Fig. 4 and support the existence of a compositional gradient in Cu* samples. Fig. 4 shows the spectra obtained for Cu 2p (a), O 1s (b) and the $L_3M_{4,5}M_{4,5}$ Auger transition (c) for samples with different Pt and Cu*. Comparing these spectra, we observe that samples with lower Cu* thickness (2nm) present a higher relative concentration in hydroxides and/or carbonates (a), as well as two clearly distinguishable components in the O 1s spectrum (b). According to their binding energy, these components can be attributed to the presence of $Cu(OH)_2$, with higher binding energy, and CuO. On the other hand, the presence of an adjacent Pt layer seems to favour the formation of CuO, as deduced from the higher contribution in the O 1s region at lower binding energies (b) and the less pronounced metallic copper features in the Auger spectrum (c).

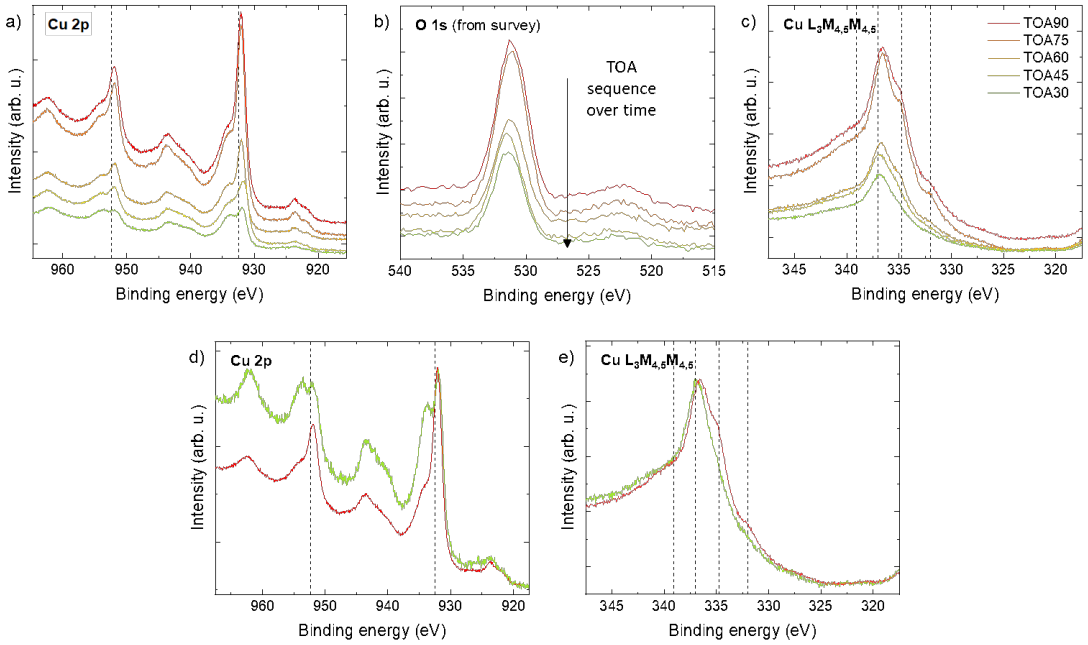

Figure 3. Take-off angle (TOA) dependence of XPS spectra collected for Co(2)|Pt(2)|Cu(3)* sample after exposure to ambient conditions for 3 days between successive measurements, for Cu 2p (a), O 1s, and the Auger $L_3M_{4,5}M_{4,5}$ transition (c). The probing depth increases with TOA being maximum for normal emission (TOA90). The time sequence of the measurements is shown in (b). The color code for all panels is shown in (c). Panels (d) and (e) compare the spectra at TOA90 (red) and TOA30 (green) for Cu 2p and the Auger $L_3M_{4,5}M_{4,5}$ transition, respectively. The intensity of these spectra (d,e) has been normalized for better comparison.

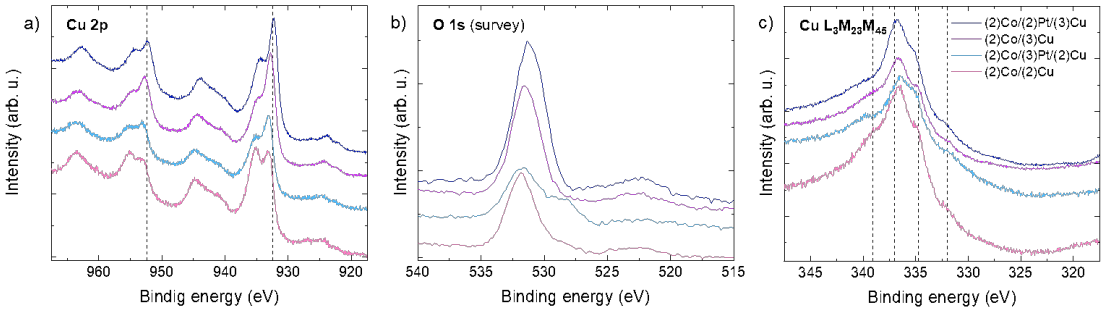

Figure 4. XPS spectra obtained for systems with different Pt and Cu* thicknesses in the Cu 2p (a), O 1s (b) and the Auger $L_3M_{4,5}M_{4,5}$ transition (c) energy region. The color code of all spectra is shown in (c).

As the Cu* thickness increases (3nm), the O 1s component previously attributed to CuO disappears (b), suggesting that it dissolves its oxygen content to form Cu_2O. As for the effect of Pt in these samples, it promotes a thickening of the oxide layer, in agreement with both the shift towards lower energies and higher intensity in the O 1s spectrum (b), and the less pronounced metallic features in the Auger $L_3M_{4,5}M_{4,5}$ energy spectrum (c).

In conclusion, these results show the subtle equilibrium between species within the spontaneously formed Cu* oxide layer. Surprisingly, we observed a phase transition as a function of the deposited Cu thickness. We found that for thinner samples (2 nm) the formation of Cu|CuO interlayers is favored, while thicker samples (3 nm) present a Cu/Cu_2O interlayer. On the other hand, we were able to deduce from these spectra a higher oxide/hydroxide ratio for samples with a Pt interlayer, most likely because in this case Cu* corrosion is more favored by the galvanic effect than in Co|Cu* samples.

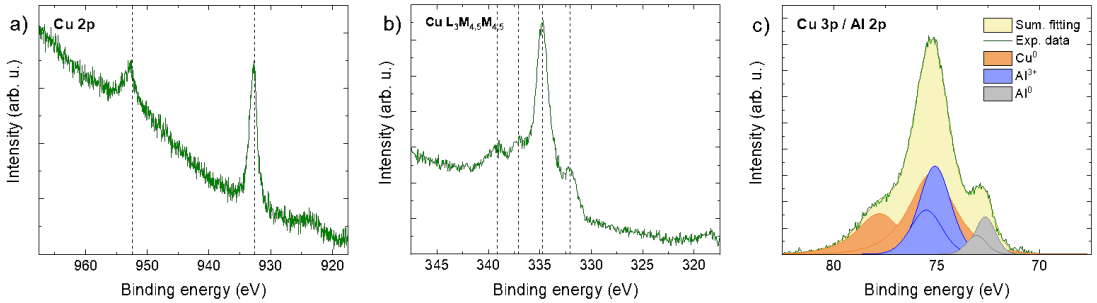

Figure 5. XPS spectra obtained for a sample Pt(8)|Co(1.4)|Cu(5)|Al(3)* by sweeping in the Cu 2p (a) and Cu 3p|Al 2p (b) energy regions. The fit of the experimental data in (b) by components obtained from reference spectra for Cu and Al* is shown in (c). The "*" denotes that the top layer was exposed to air. The color code of all spectra is shown in (c).

B. Pt|Co|Cu|Al* samples

In this last section we discuss the spectra obtained for Pt(8)|Co(1.4)|Cu(5)|Al(3)*. Panels (a) and (b) in Fig. 5 show, respectively, the Cu 2p and the Auger transition $L_3M_{4,5}M_{4,5}$ energy regions, confirming the sole presence of metallic Cu. Thanks to Cu and Al* reference spectra, we can fit the experimental data as shown in (c) for the Cu 3p and Al 2p energy region. We find a good fit when considering the presence of metallic Al together with Al_2O_3. Furthermore, using a series of Al samples of varying thickness on which reflectometry and XPS measurements have been performed, we were able to estimate the remaining metallic Al thickness at about 3nm. From the above, we can conclude that the distribution across the Al* layer in Pt(8)|Co(1.4)|Cu(5)|Al(3)* is metallic Al|Al_2O_3.

II. THZ-TDS SPECTROSCOPY MEASUREMENTS

Concerning the THz spectroscopy experiments (THz-TDS) in the so-called emission mode, we used ultrafast NIR pulses ($\simeq$ 100 fs) centered at λ_{NIR}=810 nm and derived from a Ti:Sapphire oscillator centered at λ_{NIR}=810 nm to photo-excite the spin carriers in Co directly from the front surface (CuOx) at a normal incidence. A standard electro-optic sampling is used to detect the electric field of the THz pulses, using a 500 μm-thick (110) ZnTe crystal. The sign change in the THz phase (not shown) demonstrates that spin (or orbital)-charge conversion (SCC) mechanisms mainly occurring in Pt is responsible for the observed THz emission. More details of the respective set-up and protocol are provided in Refs. [7–11].

The observed shape of the E_{THz} *vs.* t_{Pt} plot results from the product of two different functions respectively $\eta \times \mathcal{A}$ involving respectively the SCC efficiency η and both the THz and NIR optical absorptions $\mathcal{A}$:

i) η is growing function of t_{Pt}, $\eta(t_{Pt}) = \theta_{SHE} \frac{g_{\uparrow\downarrow} r_s \tanh\left(\frac{t_{Pt}}{2\lambda_{sf}^{Pt}}\right)}{1+g_{\uparrow\downarrow} r_s \coth\left(\frac{t_{Pt}}{\lambda_{sf}^{Pt}}\right)}$ passing through the origin ($\eta = 0$ for $t_{Pt} = 0$).

The λ_{sf}^{Pt} is the hot electron spin relaxation length in Pt, the typical lengthscale over which the ISHE occurs; $r_s = \rho_{Pt} \times \lambda_{sf}^{Pt}$ is the corresponding spin resistance of Pt [7] (we will further call $\tilde{r}_s = g_{\uparrow\downarrow} r_s$, the reduced spin resistance by multiplication with the spin-mixing conductance),

ii) $\mathcal{A}$ is a certain decreasing function of t_{Pt}: $\mathcal{A} \propto \exp\left(-\frac{t_{Pt}}{\Lambda_{NIR}^{Pt}}\right)\left(\frac{Z_0}{1+n_{subs.}+Z_0 \int \sigma dt}\right)$ related to the optical NIR pump and THz absorption processes respectively [9, 12]. Here, $Z_0 = \sqrt{\frac{\mu_0}{\epsilon_0}}$ is the vaccuum impedance where μ_0 is the magnetic permeability and ϵ_0 the dielectrical constant in vaccuum. σ is the layer metallic conductivity, t the thickness (dt means the integral within the thickness, $n_{subs.}$ is the optical index of the substrate in the THz window and $\Lambda_{NIR}^{Pt} \simeq 12$ nm is the typical optical absorption length in Pt in the near-infrared (NIR) window. The $\exp(-\frac{t_{Pt}}{\Lambda_{NIR}^{Pt}})$ prefactor then takes into account the decrease variation of the optical excitation in Co due to the Pt layer. The remaining part $\frac{Z_0}{1+n_{subs.}+Z_0 \int \sigma dt}$ is related to the THz absorption within the thin metallic multilayers in the stack [12] and as discussed in the main text.

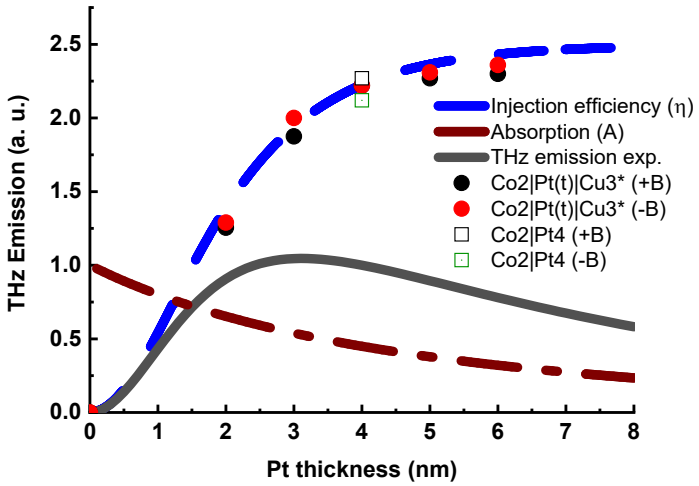

Figure 6. THz data: (Black line) fitting of the experimental E_{THz} data corresponding to the $(\mathcal{A}(t_{\mathrm{Pt}}) \times \eta(t_{\mathrm{Pt}}))$ product. (brown dash line) NIR plus THz Optical absorptions $(\mathcal{A}(t_{\mathrm{Pt}})$ function). (blue dashed) spin injection efficiency extracted from experiments $(\eta(t_{\mathrm{Pt}})$ by removing the optical absorption. (color circles) Experimental data of the spin injection efficiency by removing the optical absorption.

The two functions, optical absorption $\mathcal{A}(t_{\mathrm{Pt}})$ (dashed brown) and THz spin injection efficiency $\eta(t_{\mathrm{Pt}})$ (blue dashed) are plotted on Fig. 6 together with the resulting product $\mathcal{A}(t_{\mathrm{Pt}}) \times \eta(t_{\mathrm{Pt}})$ (black). The experimental data points renormalized from the optical absorption are shown by color circles. The data analyses have been performed by considering material conductivities: $\sigma_{\mathrm{Pt}} = 4 \times 10^6$ S/m (resitivity $\rho_{\mathrm{Pt}} = 25\ \mu\Omega$.cm), $\sigma_{Co} = 2 \times 10^6$ S/m ($\rho_{\mathrm{Co}(2)} = 50\ \mu\Omega$.cm) and $\sigma_{Cu} = 10^7$ S/m (resitivity $\rho_{\mathrm{Cu}} = 10\ \mu\Omega$.cm) and thickness $t_{\mathrm{Cu}} = 1$ nm.

III. ANOMALOUS AND PLANAR HALL EFFECT MEASUREMENTS

In our samples, the anisotropy and amplitude of anomalous Hall resistance (R_{AHE}) are determined by measuring the Hall resistance (R_H) as a function of the out-of-plane magnetic field (H_z). A typical example of such a measurement in Si|SiO_2|Co(2)|Pt(4)|Cu*(3) is shown in Fig.7(a). As expected, the Hall resistance exhibits a linear increase with the magnetic field, saturating after reaching a certain magnetic field strength. The field at which the R_H saturates is defined as the anisotropy field (H_k) and the saturated R_H value corresponds to R_{AHE}, as indicated by the blue arrows in the figure.

The R_{PHE} values are obtained by measuring the R_H as a function of the in-plane angle between magnetization and current under a constant in-plane magnetic field (700 mT in for this case). In Fig. 7b, we present the variation of R_H (black points) in Si|SiO_2|Co(2)|Pt(4)|Cu*(3) as a function of the rotation angle. The R_H shows a typical angle dependency according to:

$$R_H = R_{PHE} \sin(2\phi) \tag{1}$$

For comparison, we also show the measurements of R_{AHE} and R_{PHE} in Si|SiO_2|Co(2)|Pt(4) (without Cu* capping layer) with . It is clearly evident from the comparison between two samples that the R_{AHE} and R_{PHE} values are higher in Si|SiO_2|Co(2)|Pt(4), indicating a significant emphasis on the current shunt path in Cu*, as emphasized in our main manuscript.

The typical values of M_s measured at squid at room temperature are $M_s = 1275$ emu/cm^3 for SiO_2|Co(2)|Pt3|Cu3* and $M_s = 1320$ emu/cm^3 for SiO_2|Co(2)|Pt4|Cu3* corresponding to a shape anisotropy of $H_s = 4\pi M_s \simeq 1.658\ T$. From the above measurements, the surface anisotropy introduced by the Co|Pt interface is about $H_{K_s} = -0.658$ T.

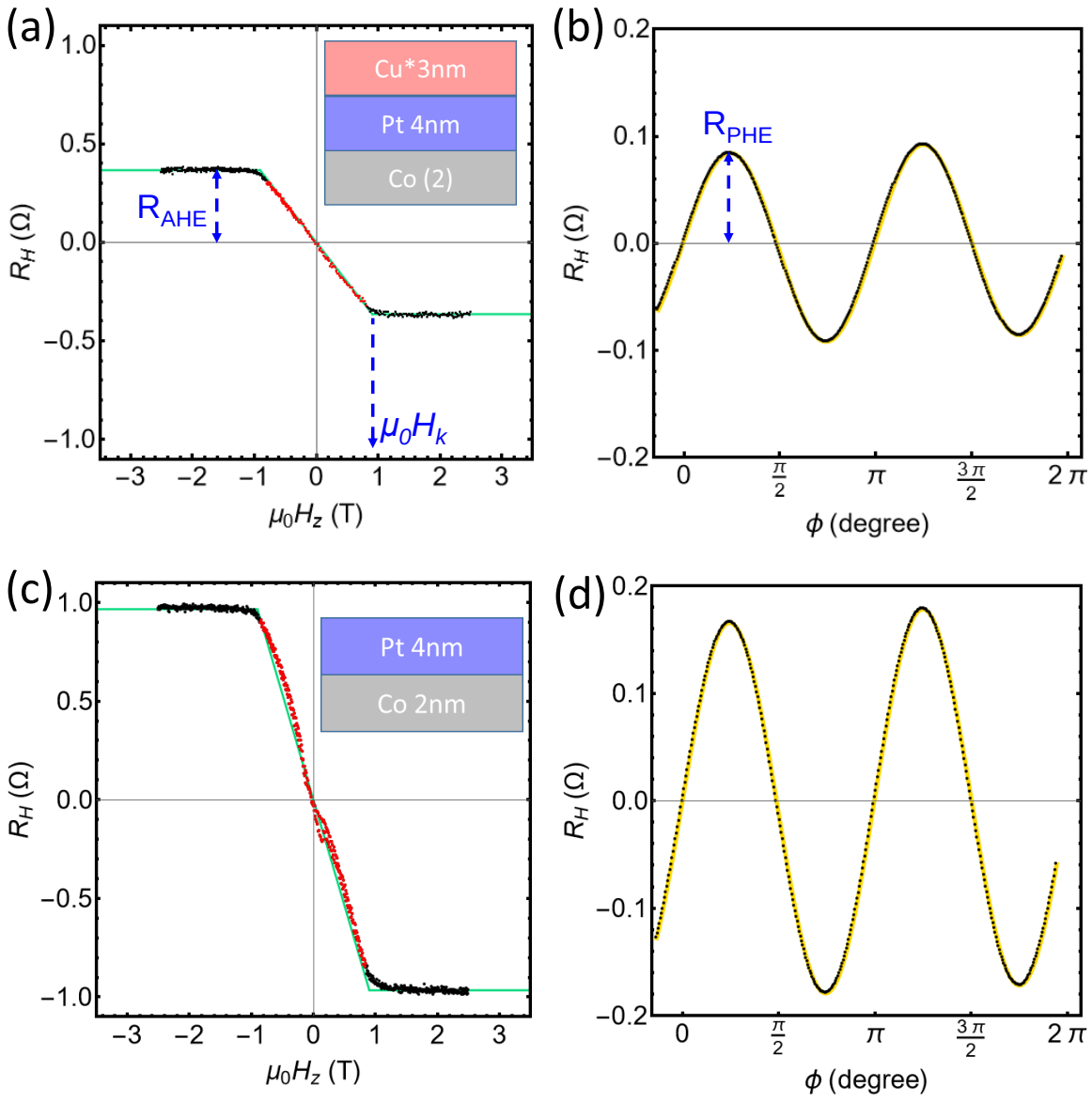

Figure 7. Measurement of R_{AHE} (in black) as a function of out-of-plane magnetic field ($\mu_0 H_z$) in (a) Si|SiO_2|Co(2)|Pt(4)|Cu*(3) and (b) Si|SiO_2|Co(2)|Pt(4). Measured Hall resistance as a function of angle between current and magnetization direction to determine the planar Hall resistance (R_{PHE}) in (b) Si|SiO_2|Co(2)|Pt(4)|Cu*(3) and (d) Si|SiO_2|Co(2)|Pt(4) samples.

IV. ORBITAL AND SPIN TRANSPORT SIMULATIONS ON $Cu|Cu|O$ AND $Cu|Al|O$

A. Electronic band structure and orbital momentum locking obtained by density functional theory (DFT).

The DFT simulations have been carried out considering two material systems. The first system is composed of thirteen layers made out from twelve Cu layers and one Oxygen layer having the same structure as that one previously studied by D. Go *et al* [13]. We used the Perdew-Burke-Ernzerhof (PBE) [14, 15] exchange-correlation functional. We perform the geometry optimizations with a plane-wave basis as implemented in the SIESTA package [16] employing an atom-centered double-ζ plus polarization (DZP) basis sets considering an energy cut-off for the real-space mesh of 350 Ry. Relativistic effects (although small in this case) are introduced via the on-site approximation [17] using fully-relativistic norm-conserving pseudopotentials [18]. The system's ground state properties are obtained after performing a full self-consistent cycle converged a $(13 \times 13 \times 1)$ $\vec{k}$-points sampling of the Brillouin zone using a 25 vacuum distance between periodic images to avoid spurious effects with the lattice constant fixed

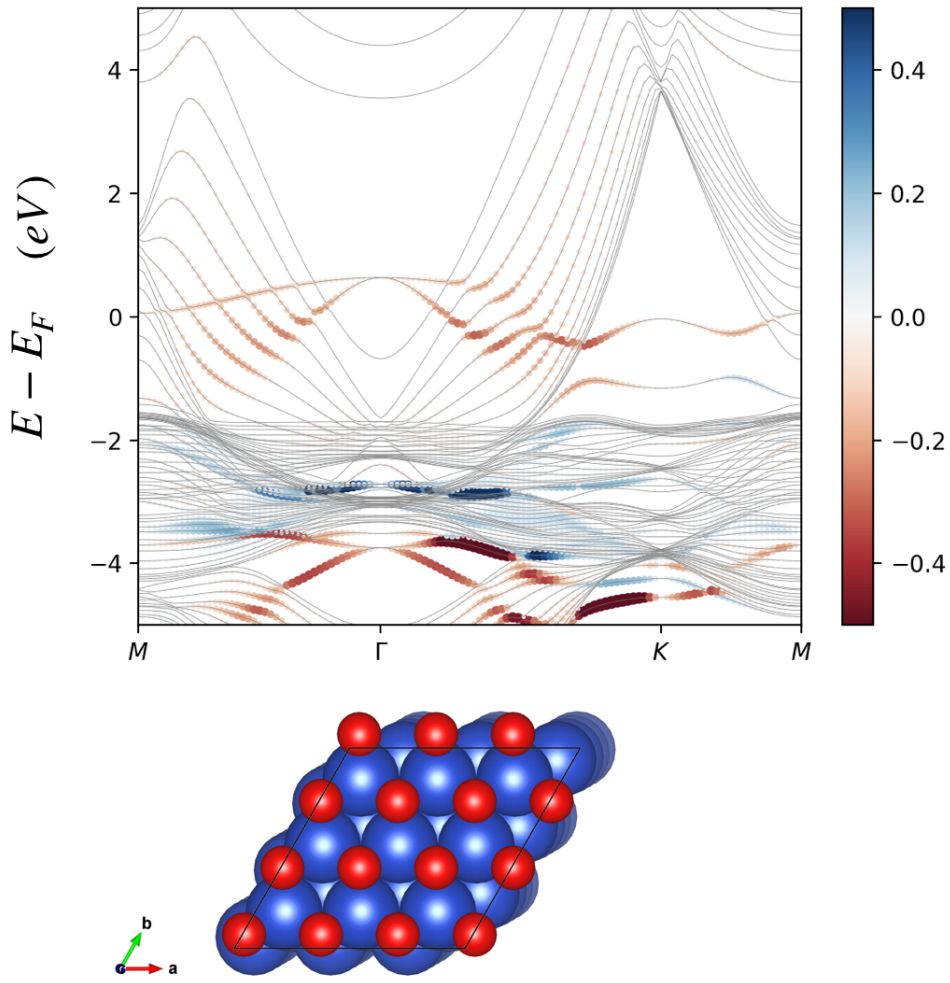

Figure 8. Electronic band structure for Cu|Cu|O showing a top view of the atomic structure within a 3×3 unit cell. The colorbar shows the orbital texture projected on the outermost Cu layer, namely $Cu_1 2$. showing the orbital polarization along the main symmetry lines.

to 2.53 Å obtained by energy minimization procedure. We have used the conjugate gradient algorithm to minimize the atomic forces below 0.01 eV/Å. The orbital texture, orbital and spin accumulations were therefore calculated by a home-made procedure using the Hamiltonian and overlap matrices.

The orbital mean value, *i.e.* orbital texture shown in Fig. 9 (a,c) have been calculated using :

$$\langle \mathbf{L}_n \rangle = \langle \psi_n | \hat{\mathbf{L}} | \psi_n \rangle \,, \tag{2}$$

where $|\psi_n\rangle$ is an eigenstate of the Hamiltonian and the overlap matrix $\hat{S}$ has to be considered as the basis is non-orthogonal. The matrices $\hat{\mathbf{L}}$ are the usual orbital angular momentum operator matrices expressed in a given atomic orbital basis, that is, p and d orbitals.

B. Orbital Rashba-Edelstein response and orbital torques obtained by density functional theory (DFT).

The spin and orbital accumulations generated by an electric field E_x applied along the $\hat{x}$ direction *via* the so-called orbital Rashba-Edelstein response χ_0 according to $\langle \psi_k | L_y | \psi_k \rangle = \chi_0 E_x$, have been calculated through the Kubo formula like proposed in Ref. [19].

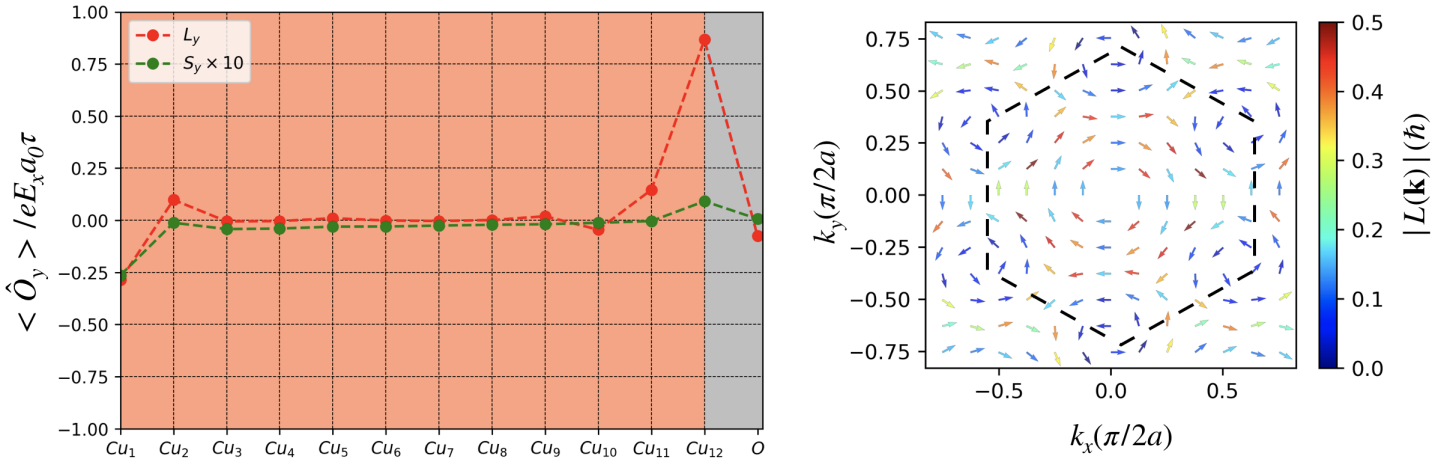

Figure 9. Orbital Rashba-Edelstein response of Cu|O in unit of $\hbar$ (left) and corresponding orbital texture for the outermost metallic layer at the Cu|O interface at the Fermi surface(right). It's worthwhile to note the strong helical property of the orbital texture (maximum of 0.8 μ_B). This is in agreement with the spin and orbital accumulations obtained for the layers, where the largest value is obtained for the Cu_{12}-th layer at the interface with the O atoms.

$$\hat{O} = -eE_x\tau \int_{BZ} \partial_\epsilon f(\epsilon) d\epsilon \, \mathrm{Re}\left[\langle\psi_n|\hat{O}|\psi_n\rangle \langle\psi_n|v_x|\psi_n\rangle\right] \tag{3}$$

where v_x is the velocity operator modified for treating a non-orthogonal basis as:

$$\mathbf{v} = \frac{\partial\hat{\mathbf{H}}}{\partial\mathbf{k}} - \frac{\varepsilon_i \partial\hat{\mathbf{S}}}{\partial\mathbf{k}}, \tag{4}$$

which for our case was taken in the $\hat{x}$ in-plane direction representing the external perturbation and $\hat{O}$ is the operator corresponding to the quantity measured *e.g.*, spin and orbital degrees of freedom. In order to extract the layer resolved spin and orbital accumulations, we project the spin and orbital operators to act only on the states originating from a given layer such that each quantity shown in Fig. 9 (b,d) is given in terms of the Bohr radius a_0 and the momentum relaxation time τ calculated for a given atomic layer. In both cases, we have considered a 150×150 mesh-grid for sampling the Brillouin Zone (BZ).

In the graphs showing a layer-by-layer resolved χ_O Rashba-Edelstein response, the values in ordinates are given in unit of $\hbar$ with the results that the amplitude of unity "1" gives a value of the order of 10^{-4}/atom. Such value has been obtained by considering a typical momentum scattering time $\tau \simeq 10^{-14}$ s and a maximum electric field of 10^5 V/m by considering a typical material resistivity $\rho = 25\mu\Omega$ cm and local current density $J = 4 \times 10^{11}$ A/m^2.

The effective damping-like field B_{DL} is then calculated by involving the dynamics of such 2-dimensional generated orbital moment transferred into the local $3d$ magnetic moment dynamics according to $\frac{\chi_0}{\tau^*}\frac{e}{a^2 m^*}E_x = \gamma B_{DL} M_s t_{co}$ or equivalently :

$$B_{DL} = \frac{\chi_0}{a^2 \tau^* M_s t_{Co}} E_x$$

where τ^* is the effective transfer time ($\tau^* = \tau$ for the maximum efficiency) from the orbit to the local magnetization and a the typical lattice parameter. We find that for $\frac{\chi_0}{ea_0\tau} \simeq \hbar$ (ordinate = "1"), $B_{DL} \simeq 15$ mT.

In order to prove the robustness of the Orbital Rashba effect in the heterostructures, we also show the Spin and Orbital accumulation and the corresponding orbital texture for electronic energy below ($\epsilon = \epsilon_f - 0.5$ eV on Fig. 10a-b) and above ($\epsilon = \epsilon_f + 0.5$ eV) the Fermi energy ϵ_F on Fig. 10c-d. We can see that for the case of Cu|O, the orbital texture displays strongly the hexagonal symmetry through all the different values of the chemical potential.

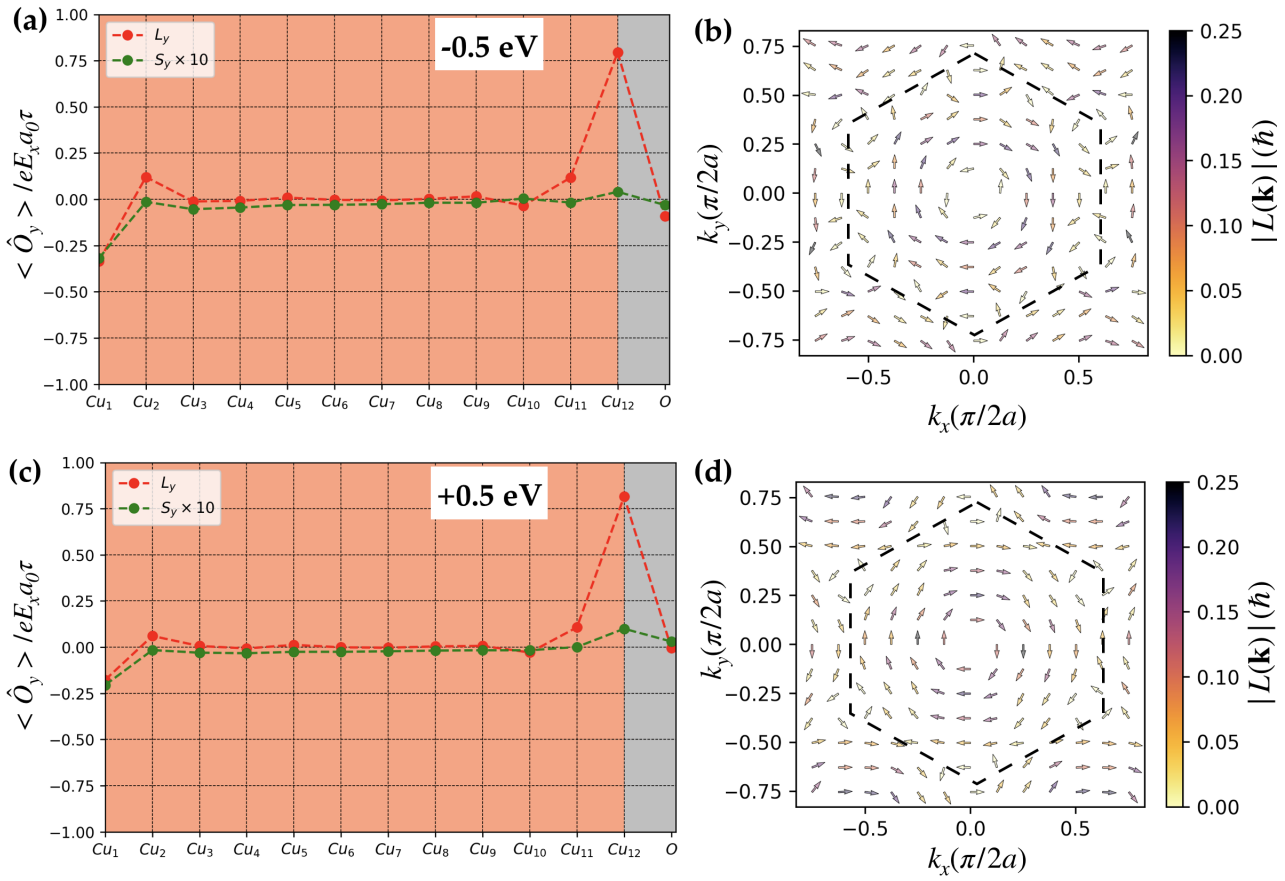

Figure 10. Orbital (spin) Rashba-Edelstein response and orbital texture for Cu|Al|O (a,b) and Cu|O (c,d) calculated at -0.5 eV.

[1] M. C. Biesinger, Advanced analysis of copper x-ray photoelectron spectra, Surface and Interface Analysis **49**, 1325 (2017).

[2] S. Lee, N. Mettlach, N. Nguyen, Y. Sun, and J. White, Copper oxide reduction through vacuum annealing, Applied Surface Science **206**, 102 (2003).

[3] A. C. Miller and G. W. Simmons, Copper by XPS, Surface Science Spectra **2**, 55 (1993).

[4] R. P. Vasquez, Cu2O by XPS, Surface Science Spectra **5**, 257 (1998).

[5] R. P. Vasquez, CuO by XPS, Surface Science Spectra **5**, 262 (1998).

[6] R. P. Vasquez, Cu(OH)2 by XPS, Surface Science Spectra **5**, 267 (1998).

[7] T. H. Dang, J. Hawecker, E. Rongione, G. Baez Flores, D. Q. To, J. C. Rojas-Sanchez, H. Nong, J. Mangeney, J. Tignon, F. Godel, S. Collin, P. Seneor, M. Bibes, A. Fert, M. Anane, J.-M. George, L. Vila, M. Cosset-Cheneau, D. Dolfi, R. Lebrun, P. Bortolotti, K. Belashchenko, S. Dhillon, and H. Jaffrès, Ultrafast spin-currents and charge conversion at 3d-5d interfaces probed by time-domain terahertz spectroscopy, Applied Physics Reviews **7**, 041409 (2020).

[8] J. Hawecker, T.-H. Dang, E. Rongione, J. Boust, S. Collin, J.-M. George, H.-J. Drouhin, Y. Laplace, R. Grasset, J. Dong, J. Mangeney, J. Tignon, H. Jaffrès, L. Perfetti, and S. Dhillon, Spin injection efficiency at metallic interfaces probed by thz emission spectroscopy, Advanced Optical Materials **9**, 2100412 (2021).

[9] J. Hawecker, E. Rongione, A. Markou, S. Krishnia, F. Godel, S. Collin, R. Lebrun, J. Tignon, J. Mangeney, T. Boulier, J.-M. George, C. Felser, H. Jaffrès, and S. Dhillon, Spintronic THz emitters based on transition metals and semi-metals/Pt multilayers, Applied Physics Letters **120**, 122406 (2022).

[10] E. Rongione, S. Fragkos, L. Baringthon, J. Hawecker, E. Xenogiannopoulou, P. Tsipas, C. Song, M. Mičica, J. Mangeney, J. Tignon, T. Boulier, N. Reyren, R. Lebrun, J.-M. George, P. Le Fèvre, S. Dhillon, A. Dimoulas, and H. Jaffrès, Ultrafast spin-charge conversion at snbi2te4/co topological insulator interfaces probed by terahertz emission spectroscopy, Advanced Optical Materials **10**, 2102061 (2022).

[11] E. Rongione, L. Baringthon, D. She, G. Patriarche, R. Lebrun, A. Lemaître, M. Morassi, N. Reyren, M. Mičica, J. Mangeney, J. Tignon, F. Bertran, S. Dhillon, P. Le Févre, H. Jaffrès, and J.-M. George, Spin-momentum locking and ultrafast spin-charge conversion in ultrathin epitaxial $bi_{1x}sb_x$ topological insulator, Advanced Science **10**, 2301124 (2023).

[12] T. Seifert, S. Jaiswal, U. Martens, J. Hannegan, L. Braun, P. Maldonado, F. Freimuth, A. Kronenberg, J. Henrizi, I. Radu, E. Beaurepaire, Y. Mokrousov, P. M. Oppeneer, M. Jourdan, G. Jakob, D. Turchinovich, L. M. Hayden, M. Wolf, M. Münzenberg, M. Kläui, and T. Kampfrath, Efficient metallic spintronic emitters of ultrabroadband terahertz radiation, Nature Photonics **10**, 483 (2016).

[13] D. Go, D. Jo, T. Gao, K. Ando, S. Blügel, H.-W. Lee, and Y. Mokrousov, Orbital rashba effect in a surface-oxidized cu film, Phys. Rev. B **103**, L121113 (2021).

[14] J. P. Perdew, J. A. Chevary, S. H. Vosko, K. A. Jackson, M. R. Pederson, D. J. Singh, and C. Fiolhais, Atoms, molecules, solids, and surfaces: Applications of the generalized gradient approximation for exchange and correlation, Phys. Rev. B **46**, 6671 (1992).

[15] J. P. Perdew, K. Burke, and M. Ernzerhof, Generalized gradient approximation made simple, Phys. Rev. Lett. **77**, 3865 (1996).

[16] J. M. Soler, E. Artacho, J. D. Gale, A. García, J. Junquera, P. Ordejón, and D. Sánchez-Portal, The siesta method for ab initio order- n materials simulation, J. Phys.: Condens. Matter **14**, 2745 (2002).

[17] L. Fernández-Seivane, M. A. Oliveira, S. Sanvito, and J. Ferrer, On-site approximation for spin–orbit coupling in linear combination of atomic orbitals density functional methods, J. Phys.: Condens. Matter **19**, 489001 (2007).

[18] N. Troullier and J. L. Martins, Efficient pseudopotentials for plane-wave calculations, Phys. Rev. B **43**, 1993 (1991).

[19] D. Go, D. Jo, T. Gao, K. Ando, S. Blügel, H.-W. Lee, and Y. Mokrousov, Orbital rashba effect in a surface-oxidized cu film, Phys. Rev. B **103**, L121113 (2021).